NRC Publications Archive
Archives des publications du CNRC

Interchangeable visual inertial LiDAR odometry and mapping payload unit for aerial vehicles

Thalagala, Ravindu G.; Gunawardana, Sahan M.; De Silva, Oscar; Mann, George K. I.; Jayasiri, Awantha; Gubbels, Arthur W.; Gosine, Raymond G.

This publication could be one of several versions: author's original, accepted manuscript or the publisher's version. / La version de cette publication peut être l'une des suivantes : la version prépublication de l'auteur, la version acceptée du manuscrit ou la version de l'éditeur.

For the publisher's version, please access the DOI link below./ Pour consulter la version de l'éditeur, utilisez le lien DOI ci-dessous.

Publisher's version / Version de l'éditeur:

https://doi.org/10.1109/ACCESS.2024.3471179

IEEE Access, 12, pp. 148904-148915, 2024-09-30

NRC Publications Archive Record / Notice des Archives des publications du CNRC :
https://nrc-publications.canada.ca/eng/view/object/?id=b0012e4f-0fee-4a02-87ab-02a62081447e
https://publications-cnrc.canada.ca/fra/voir/objet/?id=b0012e4f-0fee-4a02-87ab-02a62081447e

Access and use of this website and the material on it are subject to the Terms and Conditions set forth at
https://nrc-publications.canada.ca/eng/copyright
READ THESE TERMS AND CONDITIONS CAREFULLY BEFORE USING THIS WEBSITE.

L'accès à ce site Web et l'utilisation de son contenu sont assujettis aux conditions présentées dans le site
https://publications-cnrc.canada.ca/fra/droits
LISEZ CES CONDITIONS ATTENTIVEMENT AVANT D'UTILISER CE SITE WEB.

Questions? Contact the NRC Publications Archive team at PublicationsArchive-ArchivesPublications@nrc-cnrc.gc.ca. If you wish to email the authors directly, please see the first page of the publication for their contact information.

Vous avez des questions? Nous pouvons vous aider. Pour communiquer directement avec un auteur, consultez la première page de la revue dans laquelle son article a été publié afin de trouver ses coordonnées. Si vous n'arrivez pas à les repérer, communiquez avec nous à PublicationsArchive-ArchivesPublications@nrc-cnrc.gc.ca.

IEEE Access
Multidisciplinary ⋮ Rapid Review ⋮ Open Access Journal

Received 30 August 2024, accepted 22 September 2024, date of publication 30 September 2024, date of current version 21 October 2024.

Digital Object Identifier 10.1109/ACCESS.2024.3471179

RESEARCH ARTICLE

Interchangeable Visual Inertial LiDAR Odometry and Mapping Payload Unit for Aerial Vehicles

RAVINDU G. THALAGALA[1], (Member, IEEE), SAHAN M. GUNAWARDANA[2], OSCAR DE SILVA[2], (Member, IEEE), GEORGE K. I. MANN[2], AWANTHA JAYASIRI[1], (Senior Member, IEEE), ARTHUR W. GUBBELS[1], AND RAYMOND G. GOSINE[2]

[1]Flight Research Laboratory, National Research Council of Canada, Ottawa, ON K1V 9B4, Canada
[2]Department of Mechanical Engineering, Memorial University of Newfoundland, St. John's, NL A1C 5S7, Canada

Corresponding author: Ravindu G. Thalagala (ravindu.thalagala@nrc-cnrc.gc.ca)

This work was supported in part by the National Research Council of Canada (NRC), in part by the Natural Sciences and Engineering Research Council of Canada (NSERC), and in part by the Memorial University of Newfoundland.

ABSTRACT This paper presents an aeronautical-grade payload unit designed for real-time execution of visual-inertial-LiDAR odometry and mapping (VILOAM) algorithms. The payload offers platform interchangeability between full-scale aircraft (e.g., Bell 412 helicopter), small-scale drones (e.g., DJI M600), and ground platforms. The use of small-scale drones renders a convenient option for the research and development of VILOAM algorithms due to the reduced resource demand and simplified pilot training, while full-scale aircraft experiments provide important operationally relevant datasets to test navigation algorithm performance for field deployment. The payload unit consists of two monocular cameras, an inertial measurement unit (IMU), a light detection and ranging (LiDAR) sensor, and a real-time kinematic (RTK) enabled global navigation satellite system (GNSS) receiver. A portable GPU interfaces with these sensors to capture hardware time-synchronized sensing data and perform real-time VILOAM, including support for AI modules for obstacle detection, emergency landing zone detection that typically occurs in field robotic applications such as last-mile goods delivery, surveillance and search and rescue flights. Field validation results for the payload unit are provided by running the developed VILOAM algorithm, as well as state-of-the-art VILOAM algorithms, and evaluating their performance in real-time localization and mapping on both platforms.

INDEX TERMS Aerial autonomy, full-scale aircraft, drones, multi sensor fusion, payload unit, visual inertial LiDAR odometry and mapping.

I. INTRODUCTION

Recent advancements in full-scale aircraft autonomy have led to research and development in various applications alongside the progression of drone technology [1], [2]. These applications encompass last-mile goods delivery [3], air taxi services [4], offshore inspections [5], and surveillance [6]. This interest is driven by the aircraft's high payload capacity, fewer regulatory restrictions in urban settings, operational safety, and extended flight durations. Notable field applications include Xwing's [7] development of an autonomous Cessna 208B for cargo delivery, Wisk's [8] progress on an autonomous air taxi drone, and Bell Vertex's [9] integration of autonomous capabilities into a Bell H130 helicopter. The autonomous operation of such platforms requires accurate localization and mapping within the operational environment to ensure safe, collision-free navigation and to facilitate emergency landing procedures when required [10].

In platform autonomy, multi-sensor fusion has become the mainstream method for enabling autonomous navigation in unmanned systems [11], [12], [13], [14], [15]. A widely

The associate editor coordinating the review of this manuscript and approving it for publication was Cheng Hu.

used example of this approach is visual-inertial-LiDAR odometry and mapping (VILOAM), which fuses data from cameras, LiDARs, and IMUs to estimate the platform's six degrees of freedom (6DOF) pose relative to its surrounding environment. In the process, a map of the environment with obstacles is generated to support safe navigation regardless of GNSS position availability. This map also facilitates the integration of trajectory planning, obstacle avoidance, and failure recovery modules, essential for real-world autonomous navigation systems.

The development of VILOAM algorithms requires sensing payloads equipped with visual, inertial, and LiDAR sensors, along with ground truth-capturing sensors such as GNSS receivers, for algorithm benchmarking purposes. Such sensor combinations are prevalent in benchmarking dataset payloads found in autonomous driving. For example, the widely popular KITTI dataset [16] features a sensing payload comprising a stereo camera, LiDAR, IMU, and GNSS receiver mounted on a car roof via railings. Similar payload configurations are found in [17] and [18], which include sensors capable of VILOAM algorithm development. These sensing payloads encompass critical features such as time synchronization, accurate sensor calibration and centimeter-level ground truth. Similar to ground platforms, these payloads can also be adapted for aerial applications. However, aerial platforms require reduced-weight payloads to withstand aggressive maneuvers and high vibrations to ensure reliable sensor operation in three-dimensional space. Therefore, the direct application of ground-based payload configurations to aerial vehicles require specific payload designs for optimal performance in the aerial domain.

Payload units capable of developing aerial VILOAM algorithms are limited in availability. The studies in [19] and [20] utilized a VILOAM capable sensing payload on a small-scale DJI M600 drone. These payloads have important characteristics such as sensor hardware time-synchronization, sensor calibration and accurate ground truth. However, these systems have experimental sensor attachments specifically optimized for the drone platform. Therefore, further modifications are required to use this sensing payload as an interchangeable unit for full-scale platforms. In contrast, the payloads utilized in full-scale platforms such as [21] and [22] are equipped with a monocular camera, IMU, and GNSS, which focus on place recognition algorithm development. They do not include LiDAR and centimetre-level ground truth positions for developing navigation algorithms such as VILOAM.

In comparison to our previous work [23], this work presents the interchangeable payload unit design that can be used between a full-scale Bell412 helicopter, a small-scale DJI M600 drone, and a car, allowing for convenient VILOAM navigation algorithm development and easily transferable testing ability between the platforms. GNSS-based hardware time-synchronization procedure, RTK GNSS ground truth, and a precise multi-sensor calibration are established to support VILOAM navigation algorithm development. Aeronautical grade platform-compliant mechanical design and a vibration isolation mount design are performed to operate on both small-scale and full-scale platforms. To validate the multi-sensor fusion performance of the payload unit, this study introduces an optimization-based factor graph architecture that fuses measurements from all sensors in the payload unit, including the camera, IMU, LiDAR, magnetometer, and RTK-GNSS receiver. Field validation results are obtained by running the developed VILOAM algorithm and state-of-the-art VILOAM algorithms in real-time, assessing their performance for localization and mapping on both platforms. The contributions of this work can be summarized as follows.

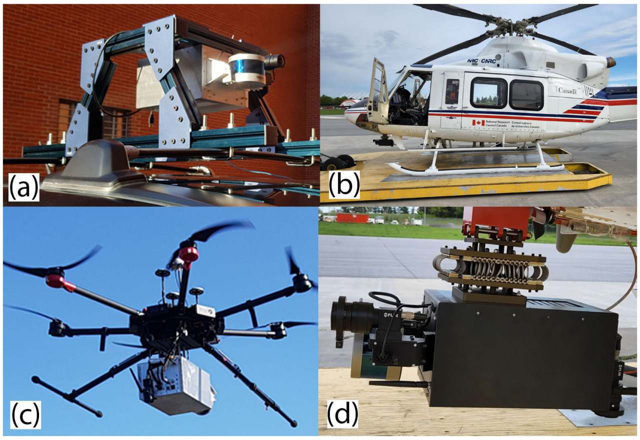

FIGURE 1. Image (a) displays the visual-inertal-LiDAR (VIL) payload unit mounted on a car, image (b) shows the payload unit installed on a DJI M600 drone, and image (c) shows the payload unit attached to the Bell412 helicopter. Image (d) provides a detailed view of the payload unit.

- Design of a visual-inertial-LiDAR payload unit that can be interchanged between full-scale aircraft, small-scale drones and ground platforms.
- Development of an aeronautical-grade mechanical structure, incorporating vibration compliance and optimized sensor selection.
- Field validation results of the payload unit, incorporating an optimization-based VILOAM algorithm using factor graph architecture and supplemented by evaluations using state-of-the-art VILOAM algorithms.

The rest of the paper is structured as follows. Section II discusses related work. An overview of the payload unit design is given in Section III. Field validation of the payload unit is presented in Section IV. Section V discusses the testing procedures for the payload unit. The results are presented in Section VI. Finally, the paper is concluded with a discussion and possible future research directions in Section VII.

II. RELATED WORK

A vast array of sensing payloads capable of VILOAM algorithm development is utilized in autonomous driving applications [16], [17], [18], [24]. VILOAM algorithms are a class of estimation algorithms that are capable of determining the 6DOF pose of a platform while simultaneously creating a map of the surrounding environment. For this purpose, payloads incorporate stereo and monocular cameras, IMUs, LiDARs, and RTK-GNSS receivers. The sensors in these systems are precisely time-synchronized and accurately calibrated, mounted on operational vehicles such as cars, which are critical for operational grade data capture. Typically, these sensors are distributed across the roof and around the vehicle, as seen in real-world autonomous driving platforms like Cruise [25] and Waymo [26]. Additionally, they are rigidly mounted to withstand platform vibrations common in real-world operations. However, these sensors are not configured into compact payload modules, as there is no requirement for further miniaturization or easy interchangeability, and they do not undergo the aggressive maneuvers typically experienced by small-scale drones or full-scale aerial platforms such as helicopters.

A few sensing payloads are available for the development of aerial VILOAM algorithms. On the small-scale drone domain, work in [19] utilized a DJI M600 drone equipped with visual-inertial-LiDAR (VIL) capable sensing payload. It contains two LiDAR scanners, a stereo camera, IMU, GNSS receiver, ultra-wideband (UWB) range sensors and laser tracker-based 3D position for ground truth. The sensors are not integrated into a single payload unit but are individually mounted at various locations on the drone. Therefore, transferring these sensors to a different platform requires further modifications. The sensing payload used in [27] has one LiDAR scanner, IMU, monocular camera, and RTK-GNSS receiver attached to a DJI M300 drone. The ground-truth data is provided using a DJI L1 payload as position, LiDAR maps, and RTK-GNSS ground truth. Similar to [19], the sensors attached to this study are also mounted in various locations to optimize space. In contrast, only a few full-scale sensing payloads are available for aerial autonomy data capture. The work in [21] used a payload with a monocular camera, IMU and GNSS receiver nose mounted on the helicopter. In [22], a sensing payload of a monocular camera, IMU and a GNSS receiver is attached to a lightweight 2-seat fixed-wing aircraft. These sensors were not assembled as a payload unit, however they were mounted as individual sensors with limited multi-sensor synchronization. Moreover, the sensing payloads in [21], [22] are intended for place recognition algorithm development and not for VILOAM navigation algorithm development.

III. PAYLOAD UNIT DESIGN

A. DESIGN CONSTRAINTS

The payload unit is designed to meet the unique design constraints of both the Bell 412 helicopter and the DJI M600 drone to ensure successful real-world operation. To be compatible with the DJI M600, the payload unit is designed weigh less than its maximum payload capacity of 7 kg. Additionally, it is designed to run on the drone's auxiliary power supply. On the other hand, the Bell 412 helicopter requires the payload unit to be able to withstand flight loads and vibrations during normal operation, and it demands specific electrical interconnects for ethernet communication and power delivery. A comprehensive list of design constraints and operational parameters is presented in Table 1.

TABLE 1. Design constraints.

Constraint	Description
Weight	7 kg
Dimensions	200(H)*150(W)*400(L)mm
Power Consumption	200 W @22 V
Operational Loads	UP:3.8 g DWN: 1.0 g LAT: 1.5 g FWD: 1.5 g AFT: 1.5 g
Operational Airspeed	FWD:70 m/s AFT:20 m/s LAT: 20 m/s
Major Frequencies	Main Rotor: 30 Hz Tail Rotor 50 Hz
Temperature	-10°C to 40°C
Relative Humidity	$\leq$ 80% (Non-Condensing)
Electrical Interconnect	Power: LEMO FGG.2B.302.52 Ethernet: LEMO FGG.2B314.62Z

B. SENSOR SETUP

In selecting the sensors for the payload unit, the VIL benchmark sensing suites such as R3LIVE [28] and LVI-SAM [11] were taken as reference. The payload unit is outfitted with sensors, including two cameras, a LiDAR scanner, an IMU, a GNSS receiver, a long-range RTK correction information receiver, and a Jetson Xavier AGX GPU. GPU integration enables the convenient integration of AI modules in the VILOAM navigation pipeline. The LiDAR is fixed in a downward-facing position, while the two cameras are fixed, one facing downwards and one facing forward. The forward-facing camera provides more information for operations at lower altitudes, whereas the downward-facing camera provides a bird's eye view of the terrain for navigation purposes at higher altitudes. The specifications of the different sensors used in the payload design are provided in Table 2.

The sensors are connected to the GPU that runs Ubuntu 18.04 with the Robot Operating System (ROS). The sensors publish data as ROS messages, recorded as a single ROS bag file. The ROS bags are saved on an internal solid-state drive (SSD) connected to the GPU to avoid streaming delays.

C. ELECTRICAL ARCHITECTURE

The electrical architecture design is centered around the necessity for hardware time-synchronized data. Along with basic functions such as power management and communication, the system is also designed to facilitate advanced

TABLE 2. Summary of sensors used in payload.

Sensor Type	Maker	Model	Rate
LiDAR	Velodyne	VLP-16	10 Hz
IMU	Xsens	MTi-30 AHRS	400 Hz
Camera-nadir	FLIR-USB	BFS-U3-16S2M-BD	20 Hz
Camera-forward	FLIR-GigE	BFS-PGE-04S2C-CS	20 Hz
Camera lens	Computar	A4Z2812CS-MPIR	-
RTK-GNSS	ArduSimple	simpleRTK2B	5 Hz
Bast station	Emlid	Reach RS2	-

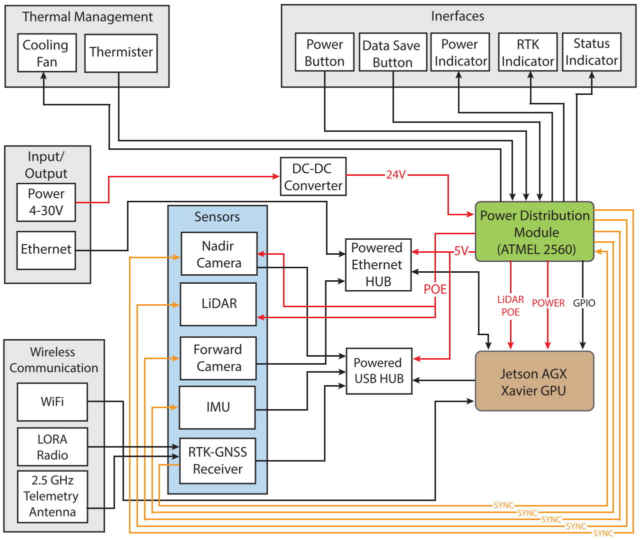

FIGURE 2. Electrical wire routing diagram.

functionalities such as routing Pulse Per Second (PPS) synchronization signals to relevant sensors.

The power distribution module (PDM) has an integrated ATmega2560 microcontroller that handles power switching to all electronics and integrates with the interface buttons and indicators. The micro-controller integrated PDM also serves device management functions like thermal management, servo control, PPS routing and conversion of NEMA GNSS messages to GPRMC format for the LiDAR. This functional data routing is used to create the wiring schematic in Figure 2. All sensors transmit data via powered Ethernet and USB hubs. These hubs also provide power to the connected sensors. The PDM hosts dedicated ports and lines for routing PPS synchronization signal to each sensor.

D. HARDWARE TIME SYNCHRONIZATION SCHEME

A PPS signal is generated by the GNSS module at a precise one-second time interval. The PDM routes the PPS signal for the sensors as indicated in Figure 3. The PPS signal synchronizes the clocks of LiDAR and IMU while synchronized IMU triggers the cameras, enabling complete time synchronization of sensors. Hence, the entire system is designed to be synchronous with the PPS signal via hardware time synchronization lines and timestamp communication with the Jetson Xavier GPU. The GPU is able to use this data to calculate absolute timestamps of the sensor trigger events. In the absence of a GNSS-generated PPS signal, the GPU can provide a simulated PPS signal to synchronize all clocks with its system clock.

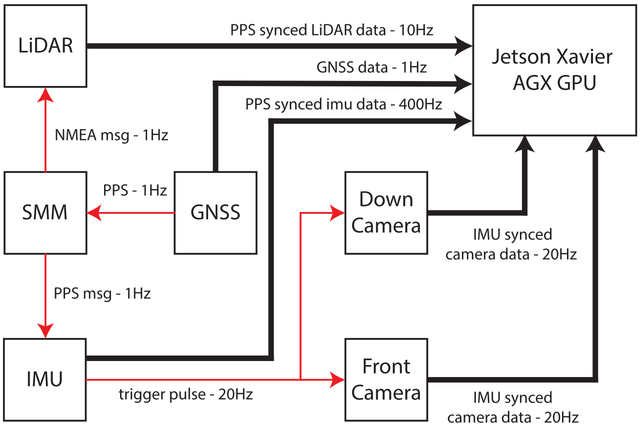

FIGURE 3. PPS time synchronization scheme.

E. MECHANICAL COMPONENTS

The payload unit is designed with a light weight casing while maintaining adequate structural strength to meet the flight-worthiness loading constraints for the Bell 412 helicopter, encapsulating all electronics. After several design iterations, the final version was designed as shown in Figure 1.

The primary load-bearing structure of the payload unit is composed of a three-member assembly, illustrated in Figure 4. This assembly serves as the main load-bearing frame, with the heaviest components directly attached to it. The frame is constructed using 5mm and 3mm sheet metal, which helps to minimize its weight. The remaining metallic components are composed of thin sheet metal, which do not contribute significantly to its strength. Finite Element Analysis (FEA) is performed on the structural assembly to ensure that an adequate factor of safety (FOS) is maintained for airworthiness.

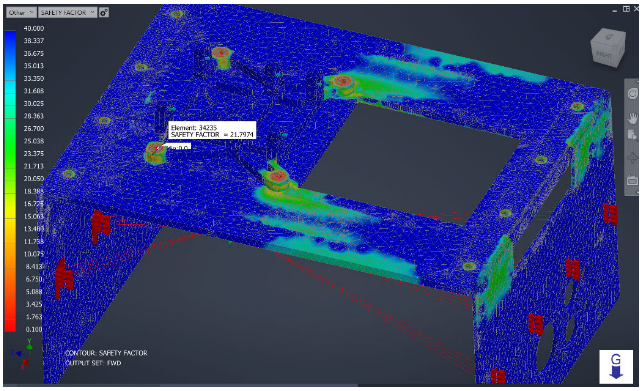

FIGURE 4. Safety factor contour plot from FEA analysis. No critically stiff areas were identified, indicating a safe design under applied loads.

The LiDAR puck is affixed to the front plate using a cradle assembly that allows it to pivot. The cradle is designed to position the LiDAR puck such that its center of gravity lies along the pivot axis. A Dynamixel servo motor powers the cradle to pivot the LiDAR puck towards areas of interest.

The payload unit addresses thermal management concerns by exposing the heat sink inlet and routing exhaust air out through a sealed passage. The design ensures that only the heat sink and fan are exposed to outside air while other electronics remain sealed. Heat-producing electronics are attached to aluminum walls with thermal paste to aid in heat conduction.

The lightweight electrical components are mounted on a mid-plate made of a 0.5mm sheet of aluminum with a stiffening member running underneath it. An adhesive-backed rubber lining is used to prevent any resonance frequencies that may be introduced during the helicopter operation.

F. FINITE ELEMENT ANALYSIS

Prior to fabrication, FEA is conducted to certify the load-bearing assembly design for flight on the NRC Bell 412 helicopter. FEA analysis of only the load-bearing assembly is considered sufficient. The final acceleration and airspeed specifications used are included in Table 1.

In FEA analysis using Autodesk Inventor Nastran, the payload was constrained in 6 dimensions by the NRC-provided mounting bracket and attached to the top plate using bolted connections with appropriate preload values. The contact criteria for the contact surface between the bracket and the top plate was a symmetric separation contact, and similar criteria were applied to connections between the forward and aft plates and the top plate. Loads were applied to the front and rear plates, taking into account their mass, attached masses, and center of gravity. The mass of the mid-plate and attached components were simulated by a concentrated mass at their center of gravity and rigidly attached to the mating surface between the mid-plate and the forward and aft plates.

Initially, conservative mesh settings were used due to limited computing resources. Instead of manual refinement, adaptive mesh refinement was used to obtain the most accurate results possible. The final mesh was obtained after 5 iterations as shown in Figure 5, with a convergence criterion of less than $< 5\%$.

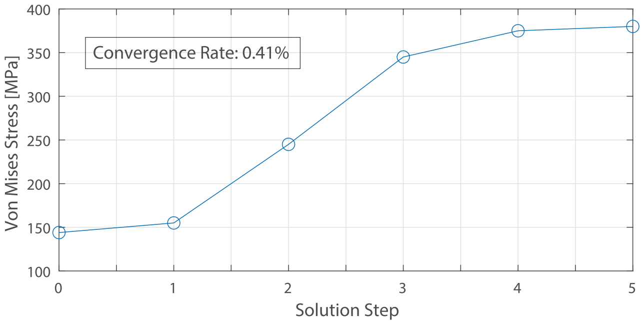

FIGURE 5. FEA adaptive meshing convergence plot.

The FEA analysis conducted shows that the stresses and strains along the expected load paths are acceptable according to airworthiness guidelines. The minimum factor of safety (FOS) for each simulation setup is considered the critical FOS for the respective loading instance. FOS contour loading is in the forward direction, with the contour range being FOS $0 - 40$.

The critical FOS results obtained from FEA analysis and their respective loading specifications are presented in Table 3. The minimum critical FOS value was found to be 8.9, which is much higher than the minimum requirement for the full-scale Bell 412 aircraft.

TABLE 3. FEA analysis results.

Subcase	Load Rating (g)	Critical FOS
UP	3.8	8.90
DWN	1.0	13.32
LFT	1.5	18.38
RHT	1.5	14.81
FWD	1.5	11.51
AFT	1.5	12.89

G. VIBRATION DAMPER DESIGN

The IMU picks up excessive vibrations as noise, which can affect its ability to generate reliable measurements. To mitigate this, a wire rope vibration isolation mount was designed to interface between the payload and the Bell412 helicopter. An Instron hydraulic actuator was used to identify the resonance frequencies of the payload. Two accelerometers were attached to the actuator and the payload to record input and resultant accelerations, as shown in Figure 6-(a).

The payload unit and the vibration isolation mount are modelled as a simple harmonic oscillator with mass m, spring stiffness k, damping coefficient c and input of $F(t)$ as shown in Figure 6 (b). The system is governed by the differential equation:

$$m\ddot{x} + c\dot{x} + kx = \mathrm{F}(t) \tag{1}$$

where $\ddot{x}$ is the acceleration, $\dot{x}$ is the velocity, x is the displacement, and $\mathrm{F}(t)$ is the external force applied to vibrate the payload. The undamped natural frequency ω_n, damping coefficient ζ, and dampened natural frequency ω_d takes the usual notation [29].

To identify the resonant frequencies of the payload unit, it was attached to a hydraulic actuator without the vibration isolation mount. The airworthiness team specified vibrations at the mounting mast were 30 Hz and 50 Hz with an amplitude of 1 mm. Therefore, a sweep of sinusoidal inputs, $F(t)$ ranging from 0 to 60 Hz with a 1 mm amplitude, was applied to the payload. The linear acceleration measured by the accelerometer indicated a resonant frequency of 54 Hz with an induced acceleration of 5 g, as shown in the root mean square (RMS) acceleration plot in Figure 7-top. The forward-looking camera lens broke off during this test due to excessive vibrations.

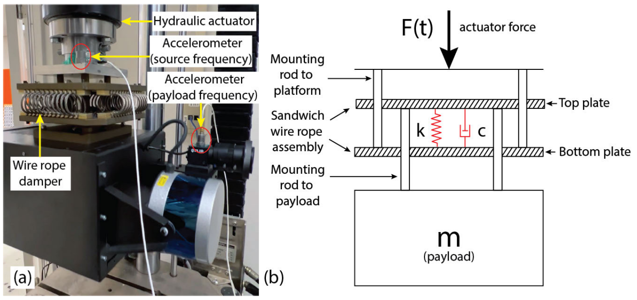

FIGURE 6. Vibration modelling and testing using the vibration machine. (a) Experimental setup (b) Simple harmonic oscillator model used to model the vibrating system.

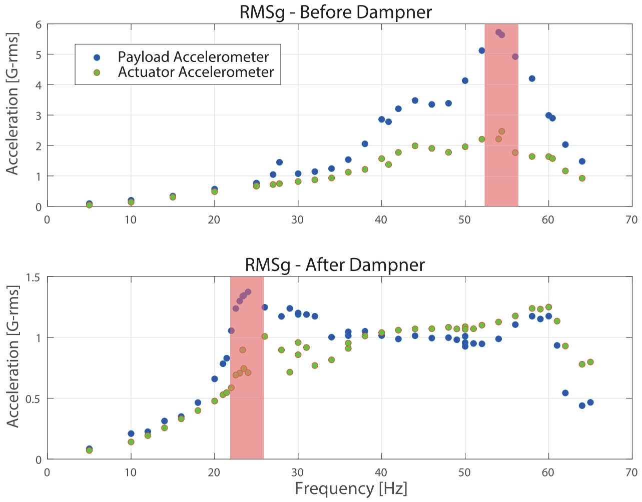

FIGURE 7. RMS acceleration comparison plot before (top) and after damper (bottom) installation. The red highlighted region indicates the peak accelerations during the tests.

To prevent sensor damage by shock loads, the objective was to lower the resonant frequency below $30\,Hz$ with induced accelerations of around 1 g. The resonant frequency of the payload was calculated as $\omega_n = 188.5$ rad/s. The corresponding spring constant k was determined as in 2.66×10^5 N/m. Assuming a damping ratio of $\zeta = 0.05$ for underdamped conditions, the damping coefficient c was calculated to be 141.37 Ns/m. The wire rope damper which was available to purchase was with $k = 1.0 \times 10^5$ N/m. Therefore, when integrated into the vibration isolation mount as shown in Figure 6, the resonant frequency observed was 23 Hz with an induced acceleration of 1.2 g as shown in Figure 7-bottom. This effectively reduced the vibrations induced on the payload below 30 Hz, ensuring the safe operation of the payload during flight.

H. SENSOR CALIBRATION

The calibration process for the payload unit involved four steps: camera intrinsic calibration using the VINS-Fusion package camera calibration tool [15], IMU intrinsic calibration using the method described in [31], camera-IMU extrinsic calibration using the Kalibr package [32], and camera-LiDAR extrinsic calibration using the Matlab LiDAR calibrator toolbox. These steps allowed us to establish the intrinsic camera parameters and the transformations between the visual inertial and LiDAR sensing units. The transformation between the RTK-GNSS antenna and the IMU was obtained from the payload unit's 3D CAD model without any optimization. They were stored as *yaml* files for running VILOAM navigation algorithms.

IV. FIELD VALIDATION OF PAYLOAD UNIT

To validate the usability of the payload unit in field applications for autonomous navigation using VILOAM algorithms, an optimization-based VILOAM is designed using factor graphs architecture, fusing the camera, IMU, LiDAR and magnetometer data, along with RTK-GNSS position measurements.

A. VILOAM ALGORITHM DESIGN

Optimization-based VILOAM algorithms, which utilize factor graphs to estimate the platform's pose and generate a map of the surrounding environment by integrating visual, inertial, and LiDAR data [15].

1) FRAME DEFINITIONS

To calculate the odometry and build a map of the surrounding environment, VILOAM uses different transformation frames illustrated in Figure 9. The body frame {B} is attached to the IMU of the moving platform. The odometry module finds the pose of {B} w.r.t. the odometry frame {O} with the origin zeroed at the start of the odometry module. The mapping module uses the mapping frame {M} to find the refined pose and register a point cloud map of the surrounding environment. The origin of {M} is zeroed at the start of the mapping module. The world frame {W} is used to reference any global measurements captured by the payload, such as GNSS, attitude and reference heading system (AHRS) readings. This work selects the East-North-Up (ENU) frame as the global frame {W}.

2) FACTOR GRAPH

In the VILOAM factor graph, each state is represented as a variable (node), and each factor is represented as an edge. A factor is a mathematical constraint applied on one or many states using sensor readings and is weighted using the noise statistics related to the sensors used for generating each factor. A factor that constraints two states is termed a "between factor", while a factor which constraint a single state is termed a "unary factor" [33], [34]. The factors used in the VILOAM algorithm include the following: the Prior Factor, which initializes the oldest state of a sliding window to maintain consistency with the previous window; the IMU Factor, which integrates high-frequency IMU measurements between factors to estimate the relative pose between states; the Odometry Factor, derived from the relative position and heading between keyframe states; the Attitude Factor, which aligns roll and pitch with the global frame; the GNSS Factor,

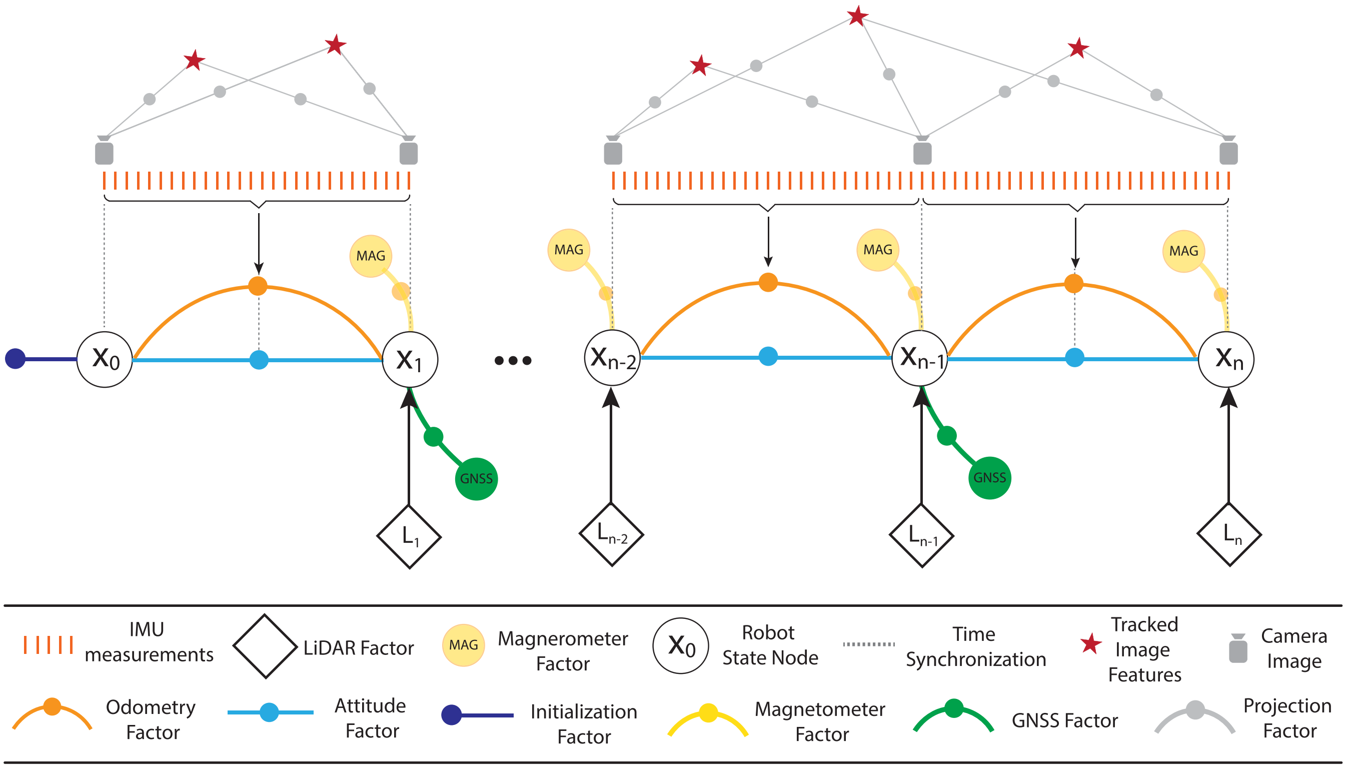

FIGURE 8. **The system structure of VILOAM. The system receives input from the camera, IMU, LiDAR, magnetometer and RTK-GNSS receiver. Five types of factors are introduced to construct the factor graph: (a) IMU pre-integration factor, (b) LiDAR factor (c) magnetometer factor, (d) Attitude factor, and (e) GNSS factor. The implementation of this factor graph can be found in [30].**

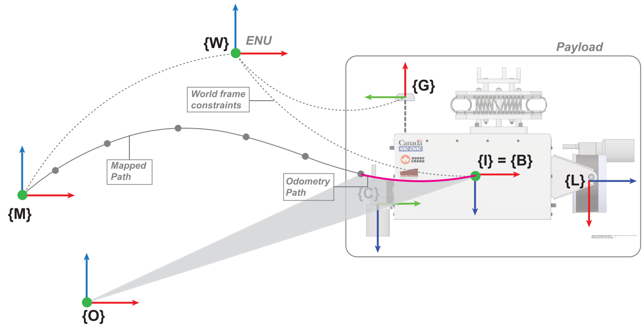

FIGURE 9. **Frame definitions of the navigation module.**

which corrects drifts using GNSS data when available; and the Magnetometer Factor, which constrains the heading with the Earth's magnetic field, employing outlier rejection to ensure robustness. A graphical representation of the factor graph is shown in Figure 8.

An optimization-based estimation framework is used in the proposed VILOAM system, which performs an online optimization of a cost function to find the least squared error agreement between all received measurements and the platform's trajectory X. The trajectory X includes N samples of the navigation state of the payload. The navigation state of the payload $\mathbf{X}_k$ consisted of $\mathbf{p}_k; \mathbf{q}_k$ of its body frame {B} relative to a navigation frame, linear velocities v_k, accelerometer bias $\mathbf{b}_a$, and gyroscope bias $\mathbf{b}_a$ for each sample k.

The VILOAM algorithm has two main modules, the odometry module and the mapping module, which are implemented as two-factor graphs. The odometry module [14] is used to solve the state at a fast rate demanded by the platform's local trajectory tracking control needs. In the odometry module, a sliding window of $n = 10$ states were maintained in the factor graph with each solved state $\mathbf{x}_k$ having the 6DOF pose of the platform $\mathbf{p}_k; \mathbf{q}_k$ w.r.t. an odometry frame $\{\mathbf{O}\}$, linear velocities $\mathbf{v}_k$, and accelerometer and gyroscope biases $\mathbf{b}_g, \mathbf{b}_a$. The mapping module is executed at a slower rate and is intended to plan the platform tasks. The mapping module factor graph only maintains the pose (position and orientation) of the platform as the state $\mathbf{X}_k$ in the mapping frame {M}. This is because the other states $(\mathbf{v}_k, \mathbf{b}_g, \mathbf{b}_a)$ are not needed by the measurement factors incorporated in the mapping module. The mapping module maintains keyframe poses corresponding to the full history of the trajectory to realize the mapping task. The complete implementation of VILOAM algorithm as a C++ ROS node can be found in [30].

V. PAYLOAD UNIT TESTING

A series of tests were conducted to verify the correct functionality of both the hardware and software modules. The primary functions of each module were independently tested to ensure proper operation, followed by integrated testing to confirm their combined functionality.

TABLE 4. Sample evaluation of datasets captured interchangeably on three platforms.

Dataset	Platform	Length [m]	Error Type	VINS-Fusion	A-LOAM	LVI-SAM	FAST-LIO2	VI-LOAM
MUN-Loop	Car	910	RMSE w.r.t GNSS [m]	28.1	34.1	fail	12.2	20.2
			RMSE angle [deg]	0.94	1.14		0.8	0.67
Lighthouse	Drone	890	RMSE w.r.t GNSS [m]	8.5	55.2	fail	7.0	8.1
			RMSE angle [deg]	11.87	104.1		10.0	11.47
Bell412-6	Helicopter	4938	RMSE w.r.t GNSS [m]	259.3	fail	fail	fail	44.76
			RMSE position [%]	5.25			fail	0.906

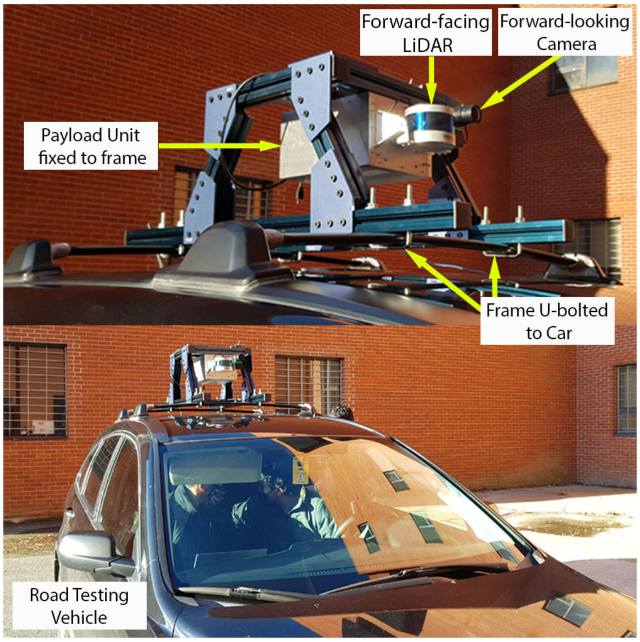

FIGURE 10. Ground platform payload unit mount with forward-facing LiDAR and camera.

A. SENSOR INTEGRATION TESTING

The testing process included bench-top flat model testing and hand-carry tests to initially troubleshoot and verify sensor data rates, hardware time synchronization, thermal performance, sensor calibration accuracy, and data visualization procedures.

1) BENCH-TOP FLAT MODEL TESTING

Bench-top flat model testing was conducted to ensure that sensor data were published at the required rates, electrical wiring and PDM operated without overheating, and hardware time synchronization functioned correctly. All ROS sensor drivers were run to publish data sequentially on the GPU and visualized using ROS Rviz to confirm that data rates were maintained without delays or interruptions. Furthermore, this test was performed for several hours to verify that the electrical wiring and PDM work without overheating.

The time synchronization scheme detailed in Section III-D was also tested using the bench-top flat model before being integrated into the payload unit. Time synchronization was achieved through the PPS signal generated by the GNSS receiver module. The LED indicator on the module blinks when PPS messages are published, and the correct functioning of the PPS was verified by ensuring that the LED indicator blinked at the PPS rate. Additionally, the RTK correction signals from the base station were confirmed by checking that the published `/fix` message status was 2. Status 2 of the fix message indicates that the ground-based augmentation connection for RTK is successfully established.

FIGURE 11. Bell412 helicopter payload mount with downward-facing LiDAR and camera.

2) ASSEMBLED PAYLOAD UNIT TESTING

After data rates, electrical properties, time synchronization and GNSS signals are verified, the flat model is assembled into the payload unit. After the sensors are rigidly mounted in the payload unit, sensor calibrations are carried out as described in Section III-H. After the sensor calibration is accurately established, state-of-the-art sensor fusion algorithms, VINS-Fusion [15], A-LOAM [35] and LVI-SAM

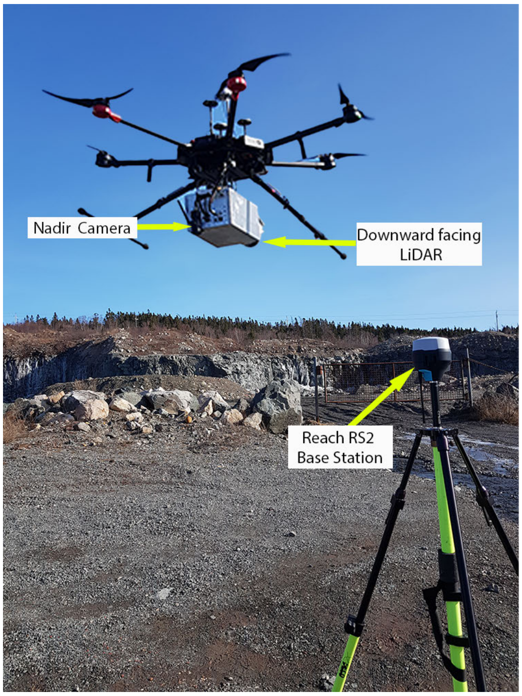

FIGURE 12. **DJI M600 small scale drone payload mount with downward-facing LiDAR and camera.**

[11] were installed in GPU and ran in parallel to test the localization performance of the payload unit before testing it on vehicles. The VINS-Fusion is used to test visual-inertial algorithm performance, and the global fusion node is used to test RTK-GNSS integration.

Additionally, VINS-Fusion enabled the calibration accuracy verification of the camera calibration and camera-IMU calibration. A-LOAM algorithm was used to test the LiDAR odometry performance. LVI-SAM is used to test the visual-inertial-LiDAR odometry and mapping performance. Additionally, camera-LiDAR calibration was also verified using this algorithm. These algorithm tests were carried out, keeping the payload unit on a cart with a total trajectory length of approximately 400m. To enable accurate RTK corrections, the GNSS base station is securely mounted outside with a clear line of sight with the sky while testing. Sensor calibrations and data rates of sensors were refined until sufficient localization performance, i.e., percentage drift with respect to root mean squared error (RMSE) of the position is less than 5%, was achieved from these algorithms as summarized in Table 4.

VI. RESULTS

The primary objective of the payload is to collect data reliably for offline algorithm testing and to run real-time navigation algorithms with easy transferability between the platforms. Interested readers can find the datasets collected from this payload unit in [23]. Three evaluations were carried out using the car, DJI M600 drone and the Bell 412 helicopter to test the interchangeability of the payload unit.

To validate the quality of the data collected, four benchmarking algorithms were utilized to evaluate the accuracy of the data produced by the payload. The four algorithms used were VINS-Fusion, A-LOAM, FAST-LIO2 [12] and the designed VI-LOAM algorithm, which is a combination of visual-inertial and LiDAR processing modules of the VINS-Fusion and A-LOAM packages respectively. Root mean squared error (RMSE) with respect to the ground truth in terms of position [m] and orientation [deg] is calculated according to [31]. [%] drift calculated by dividing RMSE by the total length travelled for both position and orientation.

A. GROUND VEHICLE EVALUATION RESULTS

The ground tests allowed for evaluating the payload unit's performance under road conditions involving aggressive translational motions, platform vibrations, and moving obstacles. These tests were conducted by rigidly mounting the payload unit on a sports utility vehicle (SUV), as shown in Figure 10. The estimation algorithms were initiated before the vehicle began moving to enable real-time localization using the payload unit. Data visualization and ROS bag recording were carried out through an Ethernet connection between the payload and a laptop inside the vehicle.

The vehicle was driven on a trajectory containing loops, and the dataset was recorded using a ROS bag, which was saved to the internal SSD of the GPU. The estimation results using the proposed VILOAM algorithm and state-of-the-art algorithms are summarized in Table 4.

The results indicate that the VINS-Fusion and VILOAM algorithms produce trajectory estimates closely aligned with the ground truth, as evidenced by the RMSE position values in Table 4. However, the LVI-SAM algorithm failed during evaluation due to the presence of moving features. The successful operation of the estimation algorithms with the payload unit demonstrates that the sensing unit functions effectively on the vehicle platform, confirming its suitability as a payload for ground platform VILOAM algorithm design.

B. DRONE EVALUATION RESULTS

To validate the suitability of the payload unit for small-scale drones, the payload unit is attached to the DJI M600 drone as shown in Figure 12. This testing also facilitated debugging and troubleshooting of the payload unit in preparation for full-scale platform aerial integration and algorithm assessment, which is challenging due to strict regulations and high costs incurred in test flights.

Several test flights were carried out in Newfoundland and Labrador, Canada, to validate the payload unit. Similar to the ground platform tests, the payload unit is initialized with estimation algorithms running in parallel before drone take-off. Also, the base station was set up in the flying area with a clear line of sight to the sky. The trajectories of the flights mimic the last-mile goods delivery scenarios to represent real world applications. The flight altitudes range from 25m–80m, covering areas including cliffs, ocean-fronts and landing zones.

The Lighthouse dataset, collected using the DJI M600 drone at St. Francis Lighthouse in Pouch Cove, NL, Canada,

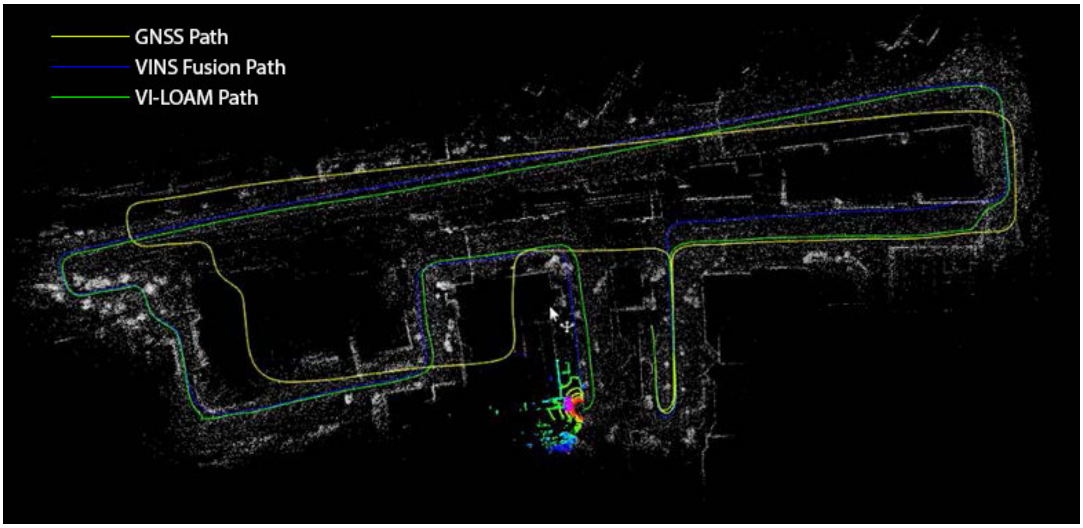

FIGURE 13. Ground platform Results: The estimated trajectories of the VINS-Fusion, VI-LOAM, RTK-GNSS positions and generated map for MUN loop dataset.

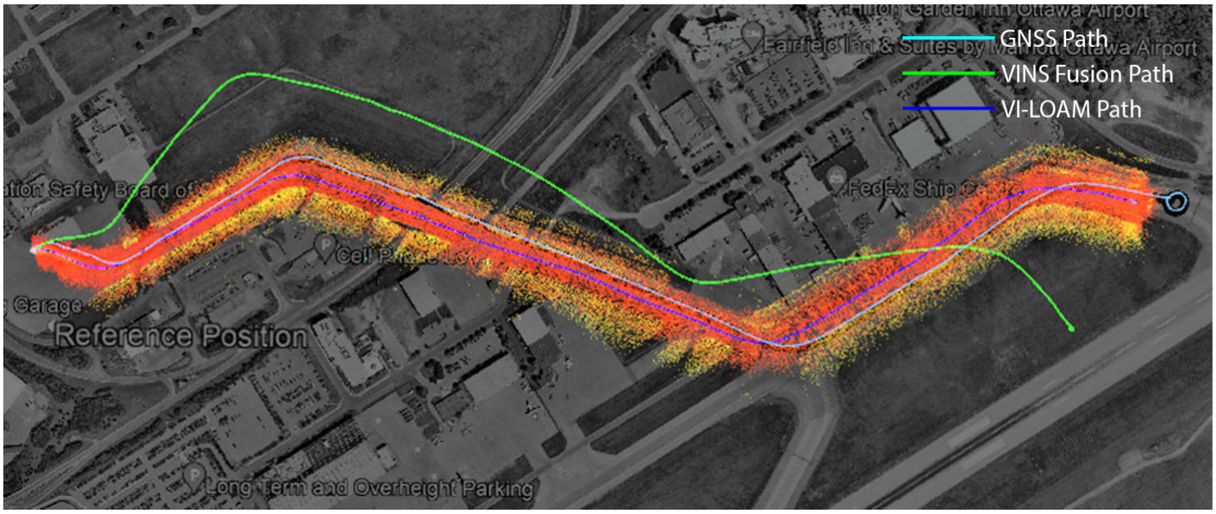

FIGURE 14. Bell412 platform results: The estimated trajectories of the VINS-Fusion, VI-LOAM, RTK-GNSS positions and generated map.

was evaluated as a sample dataset. All considered estimation algorithms successfully estimated the trajectory of the Lighthouse dataset. The estimated trajectories are closely aligned with the ground truth, as shown in the estimation accuracy results summarized in Table 4. The flight trajectory, generated map and VILOAM path comparison plot are shown in Figure 15.

C. HELICOPTER EVALUATION RESULTS

The payload unit was attached to the Bell-412 helicopter after completing the tests using a car and DJI M600 drone as shown in Figure 11. Before the helicopter took off, the data collection and estimation algorithms were initiated using an Ethernet connection through the aircraft network. Data visualization was conducted via the payload's WiFi connection, allowing real-time observation of the algorithm's localization performance.

Several test flights were conducted with the helicopter in the vicinity of Ottawa International Airport, ON, Canada. These flights, designed to simulate last-mile goods delivery, involved varying altitudes, ranging from low-altitude flights at 25m to high-altitude flights at 150m. The test runs covered diverse environments, including urban areas, highways, prairies, and runways.

The Bell 412 testing predominantly experienced high-magnitude vibrations, especially during take-off and landing. The test flights also covered flat terrains, such as runways and prairies. Despite the vibrations and featureless terrain, VINS-Fusion, VILOAM, and FAST-LIO successfully estimated the trajectories with close alignment to the ground truth, as shown in Table 4. The flight trajectory, generated map and the VI-LOAM path comparison plots are shown in Figure 14.

VII. CONCLUSION

This study presented the design and implementation of an interchangeable payload unit suitable for both full-scale and small-scale aerial platforms and ground platforms, specifically for VILOAM algorithm development. The payload

(a) Lighthouse dataset GNSS path

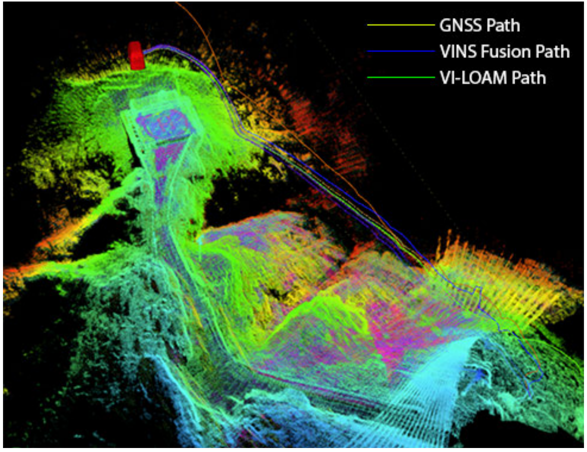

(b) VIL mapping result

FIGURE 15. **DJI M600 results: VILOAM results on the lighthouse dataset. (a) Google map of trajectory. (b) VILOAM Map and odometry paths.**

unit was custom-designed to ensure vibration compliance across aerial and ground platforms. This included creating and testing a custom vibration isolation mount for a full-scale Bell412 helicopter. Field experiments were conducted to validate the payload unit's capability on various platforms, demonstrating its effectiveness in producing LiDAR maps and delivering accurate localization results. Future work will focus on integrating high-resolution LiDAR scanners, such as the Livox Avia, to enhance the scanning resolution of the payload. This improvement aims to increase the VILOAM algorithm's accuracy further, thereby expanding the potential applications and reliability of the payload unit across diverse operational environments.

ACKNOWLEDGMENT

The authors would like to acknowledge the development and testing support of the Flight Research Laboratory—National Research Council of Canada and the Intelligent Systems Laboratory—Memorial University of Newfoundland.

REFERENCES

[1] J.-H. Kim and S. Sukkarieh, "Airborne simultaneous localisation and map building," in *Proc. IEEE Int. Conf. Robot. Autom.*, vol. 1, Jul. 2003, pp. 406–411.

[2] N. S. Labib, M. R. Brust, G. Danoy, and P. Bouvry, "The rise of drones in Internet of Things: A survey on the evolution, prospects and challenges of unmanned aerial vehicles," *IEEE Access*, vol. 9, pp. 115466–115487, 2021.

[3] V. R. F. Miranda, A. M. C. Rezende, T. L. Rocha, H. Azpúrua, L. C. A. Pimenta, and G. M. Freitas, "Autonomous navigation system for a delivery drone," *J. Control, Autom. Electr. Syst.*, vol. 33, no. 1, pp. 141–155, Feb. 2022.

[4] Z. Pei, T. Fang, K. Weng, and W. Yi, "Urban on-demand delivery via autonomous aerial mobility: Formulation and exact algorithm," *IEEE Trans. Autom. Sci. Eng.*, pp. 1–15, 2004.

[5] J.-P. Aurambout, K. Gkoumas, and B. Ciuffo, "Last mile delivery by drones: An estimation of viable market potential and access to citizens across European cities," *Eur. Transp. Res. Rev.*, vol. 11, no. 1, pp. 1–21, Dec. 2019.

[6] A. P. Cohen, S. A. Shaheen, and E. M. Farrar, "Urban air mobility: History, ecosystem, market potential, and challenges," *IEEE Trans. Intell. Transp. Syst.*, vol. 22, no. 9, pp. 6074–6087, Sep. 2021.

[7] *How Xwing is Bringing End-to-End Autonomous Flight*. [Online]. Available: https://simpleflying.com/how-xwing-is-bringing-end-to-end-autonomous-flight/

[8] Wisk. (2024). *Autonomy|Wisk*. [Online]. Available: https://wisk.aero/autonomy/

[9] M. Beul and S. Behnke, "Analytical time-optimal trajectory generation and control for multirotors," in *Proc. Int. Conf. Unmanned Aircr. Syst. (ICUAS)*, Jun. 2016, pp. 87–96.

[10] X. Yang and P. Wei, "Autonomous free flight operations in urban air mobility with computational guidance and collision avoidance," *IEEE Trans. Intell. Transp. Syst.*, vol. 22, no. 9, pp. 5962–5975, Sep. 2021.

[11] T. Shan, B. Englot, C. Ratti, and D. Rus, "LVI-SAM: Tightly-coupled LiDAR-visual-inertial odometry via smoothing and mapping," in *Proc. IEEE Int. Conf. Robot. Autom. (ICRA)*, May 2021, pp. 5692–5698.

[12] W. Xu, Y. Cai, D. He, J. Lin, and F. Zhang, "FAST-LIO2: Fast direct LiDAR-inertial odometry," *IEEE Trans. Robot.*, vol. 38, no. 4, pp. 2053–2073, Aug. 2022.

[13] T. Shan, B. Englot, D. Meyers, W. Wang, C. Ratti, and D. Rus, "LIO-SAM: Tightly-coupled LiDAR inertial odometry via smoothing and mapping," in *Proc. IEEE/RSJ Int. Conf. Intell. Robots Syst. (IROS)*, Oct. 2020, pp. 5135–5142.

[14] T. Qin, P. Li, and S. Shen, "VINS-mono: A robust and versatile monocular visual-inertial state estimator," *IEEE Trans. Robot.*, vol. 34, no. 4, pp. 1004–1020, Aug. 2018.

[15] T. Qin, J. Pan, S. Cao, and S. Shen, "A general optimization-based framework for local odometry estimation with multiple sensors," 2019, *arXiv:1901.03638*.

[16] A. Geiger, P. Lenz, C. Stiller, and R. Urtasun, "Vision meets robotics: The KITTI dataset," *Int. J. Robot. Res.*, vol. 32, no. 11, pp. 1231–1237, Sep. 2013.

[17] W. Maddern, G. Pascoe, C. Linegar, and P. Newman, "1 year, 1000 km: The Oxford RobotCar dataset," *Int. J. Robot. Res.*, vol. 36, no. 1, pp. 3–15, Jan. 2017, doi: 10.1177/0278364916679498.

[18] J. Jeong, Y. Cho, Y.-S. Shin, H. Roh, and A. Kim, "Complex urban dataset with multi-level sensors from highly diverse urban environments," *Int. J. Robot. Res.*, vol. 38, no. 6, pp. 642–657, May 2019, doi: 10.1177/0278364919843996.

[19] T.-M. Nguyen, S. Yuan, M. Cao, Y. Lyu, T. H. Nguyen, and L. Xie, "NTU VIRAL: A visual-inertial-ranging-LiDAR dataset, from an aerial vehicle viewpoint," *Int. J. Robot. Res.*, vol. 41, no. 3, pp. 270–280, Mar. 2022, doi: 10.1177/02783649211052312.

[20] C. Zheng, Q. Zhu, W. Xu, X. Liu, Q. Guo, and F. Zhang, "FAST-LIVO: Fast and tightly-coupled sparse-direct LiDAR-Inertial-Visual odometry," in *Proc. IEEE/RSJ Int. Conf. Intell. Robots Syst. (IROS)*, Oct. 2022, pp. 4003–4009.

[21] I. Cisneros, P. Yin, J. Zhang, H. Choset, and S. Scherer, "ALTO: A large-scale dataset for UAV visual place recognition and localization," 2022, *arXiv:2207.12317*.

[22] M. Schleiss, F. Rouatbi, and D. Cremers, "VPAIR—Aerial visual place recognition and localization in large-scale outdoor environments," 2022, *arXiv:2205.11567*.

[23] R. G. Thalagala, O. De Silva, A. Jayasiri, A. Gubbels, G. K. Mann, and R. G. Gosine, "MUN-FRL: A visual-inertial-LiDAR dataset for aerial autonomous navigation and mapping," *Int. J. Robot. Res.*, Apr. 2024.

[24] P. Wenzel, R. Wang, N. Yang, Q. Cheng, and Q. Khan, "4Seasons: A cross-season dataset for multi-weather SLAM in autonomous driving," in *Proc. DAGM German Conf. Pattern Recognit.*, in Lecture Notes in Computer Science: Including Subseries Lecture Notes in Artificial Intelligence and Lecture Notes in Bioinformatics, vol. 12544, 2020, pp. 404–417.

[25] Cruise. (2024). *Cruise Self Driving Cars | Autonomous Vehicles | Driverless Rides & Delivery*. [Online]. Available: https://www.getcruise.com/

[26] Waymo. (2024). *Waymo—Self-Driving Cars—Autonomous Vehicles—Ride-Hail*. [Online]. Available: https://waymo.com/

[27] H. Li, Y. Zou, N. Chen, J. Lin, X. Liu, W. Xu, C. Zheng, R. Li, D. He, F. Kong, Y. Cai, Z. Liu, S. Zhou, K. Xue, and F. Zhang, "MARS-LVIG dataset: A multi-sensor aerial robots SLAM dataset for LiDAR-visual-inertial-GNSS fusion," *Int. J. Robot. Res.*, vol. 43, no. 8, pp. 1114–1127, Jul. 2024.

[28] J. Lin and F. Zhang, "R3LIVE: A robust, real-time, RGB-colored, LiDAR-inertial-visual tightly-coupled state estimation and mapping package," in *Proc. Int. Conf. Robot. Autom. (ICRA)*, May 2022, pp. 10672–10678.

[29] F. Wang, S. Zheng, C. Huang, W. Wang, J. Yan, Z. He, H. Yu, and J. Liao, "Research and application of vibration isolation platform based on nonlinear vibration isolation system," *J. Sensors*, vol. 2023, no. 1, Jan. 2023, Art. no. 9967142.

[30] D. T. Dissanayake, S. M. Gunawardhana, O. De Silva, G. K. Mann, and R. G. Gosine. *VI-LOAM_ISLAB*. [Online]. Available: https://github.com/didzdissanayaka8/VI-LOAM

[31] D. Schubert, T. Goll, N. Demmel, V. Usenko, J. Stückler, and D. Cremers, "The TUM VI benchmark for evaluating visual-inertial odometry," 2018, *arXiv:1804.06120*.

[32] P. Furgale, J. Rehder, and R. Siegwart, "Unified temporal and spatial calibration for multi-sensor systems," in *Proc. IEEE/RSJ Int. Conf. Intell. Robots Syst.*, Nov. 2013, pp. 1280–1286.

[33] F. Dellaert and M. Kaess, "Factor graphs for robot perception," *Found. Trends Robot.*, vol. 6, nos. 1–2, pp. 1–139, 2017.

[34] K. B. Tennakoon, "Place recognition and factor graph localization for mobile robots using Google indoor street view," Ph.D. dissertation, 2021.

[35] *GitHub-HKUST-Aerial-Robotics/A-LOAM: Advanced Implementation of LOAM*. [Online]. Available: https://github.com/HKUST-Aerial-Robotics/A-LOAM

RAVINDU G. THALAGALA (Member, IEEE) received the B.Sc. degree in mechanical engineering from the University of Moratuwa, Sri Lanka, in 2016, and the M.Sc. and Ph.D. degrees in mechanical engineering from the Memorial University of Newfoundland, in 2019 and 2024, respectively. His research interests include state estimation, localization sensor development, and the development of multi-sensor fusion algorithms for aerial robotic platforms.

SAHAN M. GUNAWARDANA is currently pursuing the bachelor's degree in mechanical engineering with the Memorial University of Newfoundland. During his engineering co-op work term, he played a key role in designing and manufacturing the multi-sensor payload unit. He is the Founder of Airntell Aerospace Inc., a company specializing in the design of fixed-wing, long-endurance unmanned aerial vehicles used for offshore search, and rescue operations. His technical research interests include aeronautical-grade mechanical design and manufacturing, vibration analysis, and PCB design.

OSCAR DE SILVA (Member, IEEE) received the B.Sc. degree in engineering from the University of Moratuwa, Moratuwa, Sri Lanka, in 2009, and the Ph.D. degree from the Memorial University of Newfoundland (MUN), St. John's, NL, Canada, in 2015. Following a postdoctoral work with the ABS Harsh Environment Technology Center, St. John's, he joined MUN as a Faculty Member, in 2016. He is currently an Associate Professor with the Faculty of Engineering and Applied Science, MUN. His main research interests include autonomous robotics, navigation system design, and machine learning.

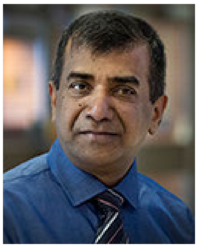

GEORGE K. I. MANN received the B.Sc. degree (Hons.) in engineering from the University of Moratuwa, Moratuwa, Sri Lanka, in 1984, the M.Sc. degree in computer-integrated manufacture from Loughborough University, Loughborough, U.K., in 1989, and the Ph.D. degree from the Memorial University of Newfoundland, St. John's, NL, Canada, in 1999. From 1999 to 2000, he was a Research Engineer with C-CORE, Memorial University of Newfoundland. In 2001, he joined the Mechanical Engineering Department, Queen's University, Kingston, ON, Canada, as a Postdoctoral Fellow. In 2002, he joined the Memorial University of Newfoundland as a Faculty Member. From 2002 to 2007, he was the C-CORE Junior Chair of Intelligent Systems of the Memorial University of Newfoundland, where he is currently a Professor of mechanical engineering with the Faculty of Engineering and Applied Science. His main research interests include intelligent control, multi-robotic systems, autonomous navigation, and robotic control.

AWANTHA JAYASIRI (Senior Member, IEEE) received the Ph.D. degree in robotics and control from Memorial University, Canada, in 2012. He was a Postdoctoral Researcher in university and an Electrical Engineer in a local company. He joined as the Research Officer of the Flight Research Laboratory, National Research Council of Canada, in 2018. His main research interests include real-time optimum control, deep learning, and computer vision in aerospace applications.

ARTHUR W. GUBBELS is a Principal Research Officer at the National Research Council of Canada's Flight Research Laboratory (FRL). He is the Facility Manager of the NRC Bell 412 Advanced Systems Research Aircraft and has managed the installation and served a crew member for the first flight of an experimental fly-by-wire research system installed in this aircraft. He is an Aeronautical Engineer with experience in handling qualities, flight controls, autonomy, data acquisition, instrumentation, computer programming, and mechanical systems. He currently leads the Flight Mechanics, Modelling and Simulation, Autonomy and Controls team at FRL.

RAYMOND G. GOSINE received the B.Eng. degree in electrical engineering from the Memorial University of Newfoundland, St. Johns, NL, Canada, and the Ph.D. degree in robotics from Cambridge University, Cambridge, U.K., in 1990. From 1991 to 1993, he was the NSERC Junior Chair of Industrial Automation and an Assistant Professor with the Department of Mechanical Engineering, The University of British Columbia, Vancouver, BC, Canada. In 1994, he joined the Faculty of Engineering, Memorial University of Newfoundland, and the Director of the Intelligent Systems Group, C-CORE. He is currently a Professor and the Associate Vice-President Researcher with the Memorial University of Newfoundland, a fellow with Canadian Institute for Advanced Research (CIFAR) Program on Innovation, Equity and the Future of Prosperity, a Fellow of Canadian Academy of Engineers (FCAE), and a Fellow of Engineers Canada (FEC).